crystals

MDPI

Article

Growth and Characterization of Centimeter-Scale Pentacene Crystals for Optoelectronic Devices

Valery A. Postnikov *, Artem A. Kulishov, Georgy A. Yurasik, Nataliya I. Sorokina, Timofei A. Sorokin and Vadim V. Grebenev

Federal Scientific Research Center "Crystallography and Photonics" of Russian Academy of Sciences, Shubnikov Institute of Crystallography, Moscow 119333, Russia; adakyla1255@gmail.com (A.A.K.); yurasik.georgy@yandex.ru (G.A.Y.); nsor@crys.ras.ru (N.I.S.); tim29@inbox.ru (T.A.S.); vadim.grebenev@gmail.com (V.V.G.)

* Correspondence: postva@yandex.ru; Tel.: +7-(985)-749-69-24

Abstract: In this work, we present results on the growth of centimeter-scale pentacene crystals using the physical vapor transport method in a dual-temperature zone horizontal furnace. It was established that intensive crystal growth processes occurred in transition regions with sudden temperature changes, while crystal growth was practically not observed in regions with slightly varying temperatures. During crystal growth, co-precipitating golden needle-like crystals reaching lengths of more than 10 mm were obtained. Using the method of single-crystal X-ray diffraction at 85 and 293 K for dark-blue lamellar pentacene crystals, the crystal structure was refined in a triclinic system with sp.gr. $P\bar{1}$. It was established that the golden needle crystals consisted of molecules of the pentacene derivative—5,14-pentacenedione, the crystal structure of which was solved for the first time in a rhombic system with sp.gr. $P2_12_12_1$. The absorption and luminescence spectra of pentacene and 5,14-pentacenedione in toluene solutions were obtained and analyzed. The electrical properties of the prepared pentacene thin films and single crystals grown under physical vapor transport conditions were evaluated by fabricating and characterizing field-effect transistors (FETs). It was shown that the presence of impurities in the commercial pentacene material had a significant effect on the morphological quality of thin polycrystalline films and noticeably reduced the hole mobility.

Keywords: pentacene; single crystal growth; physical vapor transport; single-crystal X-ray diffraction; crystal structure; 5,14-pentacenedione; optical spectra; electrical properties; field-effect transistor

check for updates

Citation: Postnikov, V.A.; Kulishov, A.A.; Yurasik, G.A.; Sorokina, N.I.; Sorokin, T.A.; Grebenev, V.V. Growth and Characterization of Centimeter-Scale Pentacene Crystals for Optoelectronic Devices. *Crystals* **2023**, *13*, 999. https://doi.org/10.3390/cryst13070999

Academic Editors: Dah-Shyang Tsai and Andreas Thissen

Received: 20 May 2023
Revised: 16 June 2023
Accepted: 19 June 2023
Published: 22 June 2023

Copyright: © 2023 by the authors. Licensee MDPI, Basel, Switzerland. This article is an open access article distributed under the terms and conditions of the Creative Commons Attribution (CC BY) license (https://creativecommons.org/licenses/by/4.0/).

1. Introduction

Pentacene (Pc) is one of the most well-known organic semiconductor compounds with good electrical properties. Due to these qualities, there is a lot of research being conducted on the development of Pc-based optoelectronic devices. In thin polycrystalline Pc layers that are thermally deposited in vacuum, the mobility, μ_h, of holes—determined by the field-effect transistor method—reaches 1.5 $cm^2 \cdot V^{-1} \cdot s^{-1}$ [1,2]. In single crystals obtained by the physical vapor transport (PVT) method, μ_h reaches values of 2.5–6.2 $cm^2 \cdot V^{-1} \cdot s^{-1}$ [3–5]. Pentacene confidently takes its rightful place in organic electronics and has not lost its popularity among research groups as a convenient material for developing new research methods [1], as a model substance [6], and also as the main or doping component in the development of optoelectronic devices [7–10].

Obtaining large samples of pentacene crystals from solutions is extremely complicated due to their low solubility in standard solvents [11,12]. Therefore, for the manufacture of organic field-effect transistors, Pc crystals are most often obtained in the form of thin polycrystalline films by thermal deposition on a substrate in vacuum [13,14]. Nonetheless, recently presented results on the growth of centimeter-scale (0.2–2 cm) Pc crystals

from a solution in naphthalene using an original high-temperature technique, which ensured satisfactory solubility of the compound, deserve attention [15]. Centimeter-scale lamellar pentacene crystals are convenient objects for studying the anisotropy of electrical properties [16].

The most accessible and relatively easy way to obtain large single crystals of pentacene is growth under PVT conditions [3,17,18]. In [19,20], while studying the growth and morphology of Pc crystals under PVT conditions, the presence of several crystal forms (needle, dendritic, lamellar) was established, and a scheme was proposed for the evolution from one crystal form to another during growth. The growth of lamellar and needle forms of pentacene crystals on substrates under PVT conditions was investigated in [5,21]. In [5], the needle-shaped crystals were identified as mixed pentacene crystals with dihydropentacene molecules, which were formed during the storage of the substance in air due to the loss of aromaticity of the inner rings.

Unfortunately, at elevated temperatures, Pc becomes less stable, which imposes special requirements on the conditions for growing crystals using the PVT method. A source with a substance must be heated to a significant temperature to create a satisfactory saturated vapor pressure [3,17,18]. It is reported that when heated, crystalline pentacene becomes unstable around 330 °C, while its thermal decomposition occurs at about 350–360 °C and above [22,23].

It seems that the methods for growing centimeter-scale Pc crystals with a desired morphology from vapor are not yet well established. This area of research is important for both fundamental and applied problems related to organic electronics. While classic setups with a gradient thermal field are more commonly used [17,24], some growth setups with several temperature zones forming a stepped thermal field profile have been explored in the literature. In particular, some studies have reported success in obtaining centimeter-scale organic semiconductor crystals using a PVT setup with two temperature zones [25–28], which allows for more precise control over the temperature field inside the growth tube compared to the gradient method. However, the regularities of crystallization under these specific conditions are still not well understood.

The aim of this work was to study the growth of centimeter-scale pentacene crystals under the conditions of physical vapor transport in a growth furnace with two temperature zones. Our attention was also drawn to the co-precipitating golden needle-shaped crystals. Previously, when studying the growth of pentacene crystals from vapor, Jo et al. also indicated the formation and growth of golden needle crystals, but their structure and chemical nature were not studied [20]. Structural analysis of this form of crystals and their optical spectra are presented in this study for the first time. The study of the electrical properties of thin polycrystalline films and large single crystals was carried out using the field-effect transistor method.

2. Experimental Section

2.1. Materials

Commercial pentacene powder (99.995%, Sigma-Aldrich, Burlington, MA, USA) was used for crystal growth without pre-purification. Studies of optical properties were carried out in spectrally pure toluene.

2.2. Differential Scanning Calorimetry (DSC) and Thermogravimetry (TG)

In order to determine the temperature range of stability and the sublimation nature of pentacene, we previously conducted a study on the thermal properties of the initial crystalline material. The experiments were carried out using aluminum sealed crucibles or those with pierced lids, and the temperature range was between 20 and 450 °C. We used the method of synchronous thermal analysis to simultaneously measure the heat flux (DSC) and mass loss (TG) using the STA 449 F1 thermoanalyzer (Netzsch, Selb, Germany). The experiments were carried out in a flow of dry nitrogen (70 mL/min) at various heating rates.

2.3. Crystal Growth and Analysis

The PVT system for growing crystals in a gradient temperature field was designed according to the classical scheme [17,24] and was used in the first stage of growth studies. A mixture of argon with 5% hydrogen (purity 99.9999%) was used as the carrier gas during crystal growth. The use of this mixture as a carrier gas was motivated by recent studies [5], which showed the positive effect of hydrogen in the growth atmosphere for the formation of the purest pentacene crystals, given its tendency toward dihydration. In all experiments, the flow rate of the carrier gas was 0.5 L/h. At this stage, the crystallization of pentacene was investigated by varying the temperature in the source region with the substance from 260 to 290 °C. At the second stage, studies were carried out on the growth of crystals in the furnace with two thermal zones: 1—hot zone for substance sublimation; 2—cold zone for deposition and growth of crystals, as originally conceived. A separate resistance furnace with independent temperature control was used for each zone. The inner diameter of the growth quartz tubes using both approaches was 19 mm. The duration of the growth period in all experiments was 72 h. The crystals were deposited both on the open surface of the quartz tube and on aluminum foil used as a substrate. The surface morphology and crystal thickness were studied using a LEXT OLS 3100 confocal microscope (Olympus, Tokyo, Japan) and an Ntegra Prima atomic force microscope (AFM) (NT-MDT, Moscow, Russia) in contact mode (probe with a cantilever rigidity of 0.03 N/m, radius of needle tip—less than 25 nm). Measurements were calibrated along the z-coordinate according to the procedure described in [12]. The resulting images were processed and analyzed using the Gwyddion program [29].

2.4. X-ray Diffraction

Single-crystal X-ray diffraction was used to study the structure of the dark-blue lamellar and golden needle single crystals. The intensity of the diffraction reflection from single crystals (size approximately 0.3 mm) was measured at temperature of 85 K on an XtaLAB Synergy-R DW system X-ray diffractometer equipped with a HyPix-Arc 150 detector (Rigaku Oxford Diffraction). The experimental data were processed using CrysAlisPro software [30]. Crystallographic calculations (correction for anomalous scattering, allowance for absorption, averaging of symmetry-equivalent reflections) were performed using the JANA2006 software package [31]. The carbon atomic coordinates were found using the charge flipping method with the Superflip program [32]. The coordinates of the non-hydrogen atoms of the structure and the parameters of their thermal displacements were specified using the least squares method in the full matrix version. The coordinates of the hydrogen atoms were fixed in the model structure either geometrically or were obtained from Fourier maps of the residual electron densities calculated in the final stage of refinement of the carbon–oxygen model. Visualization and analysis of the crystal structure were performed using the Mercury software package [33]. Calculating the potentials of pair interactions between the nearest molecules in the crystal was performed on the basis of the force field using the 'UNI Intermolecular Potentials' component in Mercury software [34].

2.5. Absorption and Luminescence Spectra

The absorption and luminescence spectra of solutions in toluene were measured in a 10 × 10 mm quartz cuvette using a Shimadzu UV-3101PC spectrophotometer and a Shimadzu RF-5301PC spectrofluorimeter, respectively. To prepare a solution of pentacene in toluene, dark-blue lamellar crystals grown in the two-zone growth setup were used. The crystals were loaded into a glass tube together with toluene and dispersed using an ultrasonic bath for 30 min at a temperature of 50 °C. Due to the low solubility of pentacene (C (20 °C) $\leq$ 0.01 g/L [12]), a homogeneous solution could not be obtained. To remove the undissolved crystals from the solution, the resulting mixture was cooled and filtered using a 0.2 μm PTFE filter. A solution in toluene with a concentration of $\leq$0.05 g/L was prepared for spectral studies of the golden needle crystals mainly formed at the exit of the cold zone of the two-zone growth furnace. The exact concentration of the solution could

not be determined due to the small amount of the substance. The solution obtained after filtration through a PTFE syringe filter with a pore size of 0.2 μm was diluted so that its optical density did not exceed 0.7 at the absorption maximum.

2.6. Elemental Analysis

Elemental analysis of the golden needle crystals was performed using a JEOL JCM-6000 Plus scanning electron microscope equipped with an energy-dispersive spectrometer (EDS) with 10 kV acceleration voltage.

2.7. Electrical Properties

The electrical properties of Pc single crystals grown by vapor and polycrystalline thin films deposited using thermal methods were studied using the field effect transistor (FET) method. FET devices with a bottom gate, top source, and drain electrodes (Figure S9a) were fabricated on 22 × 22 mm p-doped silicon wafers that were 0.5 mm thick and coated with a 440 nm thick layer of silicon oxide (SiO_2) formed through annealing, which acted as a gate dielectric. On one side of the silicon wafers, the SiO_2 layer was removed by etching with hydrofluoric acid (HF). The substrates were subsequently cleaned with acetone, isopropanol, and deionized water, kept for 0.5 h in a mixture of sulfuric acid (50%), hydrogen peroxide (20%), and water (30%), washed with deionized water, and dried with a stream of argon.

To investigate the properties of individual Pc single crystals, a layer of poly(methyl methacrylate) (PMMA) was deposited onto the surface of the SiO_2 substrate from a toluene solution using spin-coating. To ensure close contact with the substrate, pentacene single crystals were pressed against it with a silicone press through a foil layer.

Thin polycrystalline Pc films, gold drain, and source contacts were deposited through shadow masks using the physical vapor deposition (PVD) method on a COVAP III platform (Angstrom Engineering, Cambridge, ON, Canada), which was integrated into a glove box and operated at a chamber pressure of 5×10^{-7} mbar. The average deposition rate of Pc and Au was about 0.5 Å/s. The thickness of the Pc and PMMA films on the substrates was determined using AFM.

The transfer and output current–voltage characteristics of the FET devices were analyzed using a 2612B SMU (Keithley, Cleveland, OH, USA) with an LA150DC probe station (Semiprobe, Winooski, VT, USA). The mobility of the charge carrier, μ_{sat}, in the saturation regime was determined based on the transfer dependency of the current value, I_{SD}, between the source and the drain from the gate voltage, V_G, obtained during measurement [35] (see Appendix A, Equation (A1)).

3. Results and Discussion

3.1. DSC and TG

DSC and TG curves for pentacene samples are presented in Figures 1 and S1. The DSC curve in Figure 1 characterizes the heating of an initial pentacene powder sample at a rate of 10 °C/min in a crucible with a pierced lid. The DSC curve exhibited a significant, broad endothermic peak with a maximum at 402 °C and an onset at approximately 320 °C. According to the literature data [22,23], this broad peak was associated with the melting, decomposition, and sublimation of the substance, and the sample lost approximately 90% of its initial mass. It should be noted that there was a minor weight loss (about 4%) of the sample within the temperature range of 280–310 °C. This inflection of the TG curve indicated a change in the mechanism of sample evaporation, which could be associated with decomposition processes on the sample surface.

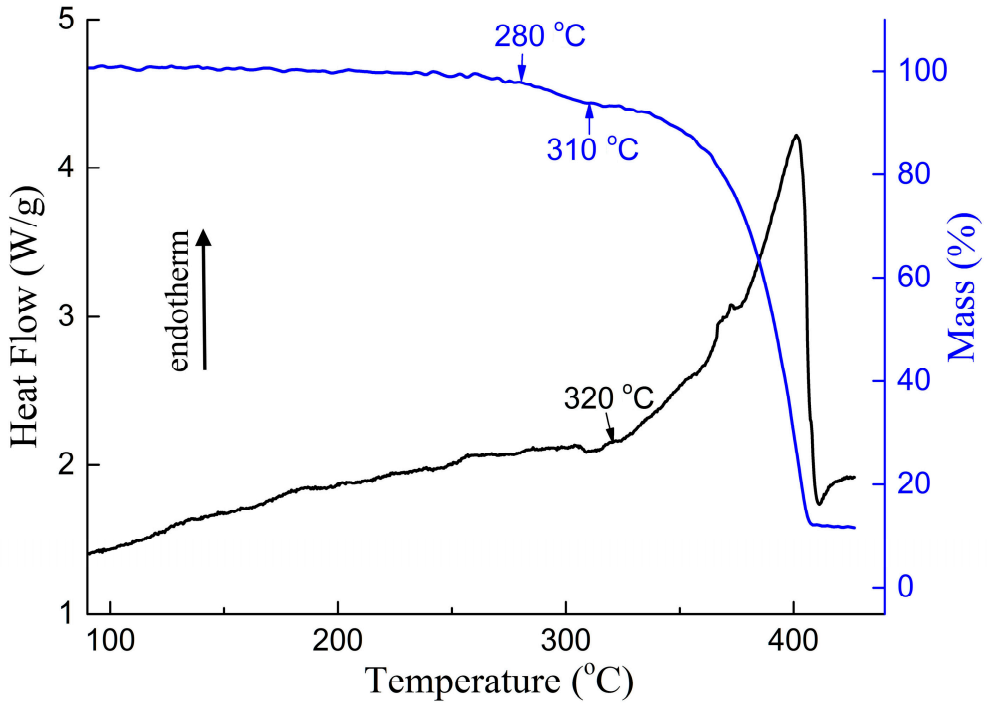


Figure 1. DSC (black) and TG curves (blue) of pentacene.

The DSC curve in Figure S1 shows the heating of a Pc sample in a sealed crucible at a rate of 50 °C/min. This high heating rate improved the signal-to-noise performance and was used to identify possible thermal effects in the material that were weak at low heating rates. As shown, two endothermic effects were observed with peaks at 370 and 375 °C. With further heating, there was competition between the endothermic processes of melting and sublimation as well as the exothermic decomposition process, which resulted in a large endothermic peak at 400 °C and a weak exothermic effect with a maximum at 408 °C (Figure 1).

Thus, based on the obtained results and the literature data [22,23], it could be concluded that during physical vapor transport in an inert atmosphere, pentacene crystals grown at source temperatures above 280 °C may have a higher probability of substance degradation.

3.2. Crystal Growth

In the first step, growth studies were conducted in a furnace with a thermal gradient field. Increasing the temperature of the source material from 260 to 290 °C resulted in nearly a two-fold increase in the average crystal concentration (cm^{-2}) within the growth zone over the same period of time.

Figure 2a depicts the relative position of the substance source and the precipitation area of dark-blue lamellar pentacene crystals (I, Figure 2b) with the temperature scale provided at the top. The largest flat sample obtained under these conditions is presented in Figure 2c. Notably, many crystals exhibited side faceting, with the angles between the side faces typically taking on several characteristic values (see Figure S2).

Next to a colony of dark-blue crystals in a colder area, the growth of golden needles up to 0.5 mm long was observed (II, Figure 2a). An enlarged image of these crystals deposited on the open surface of a quartz growth tube at a source temperature of 290 °C is shown in Figure 2d.

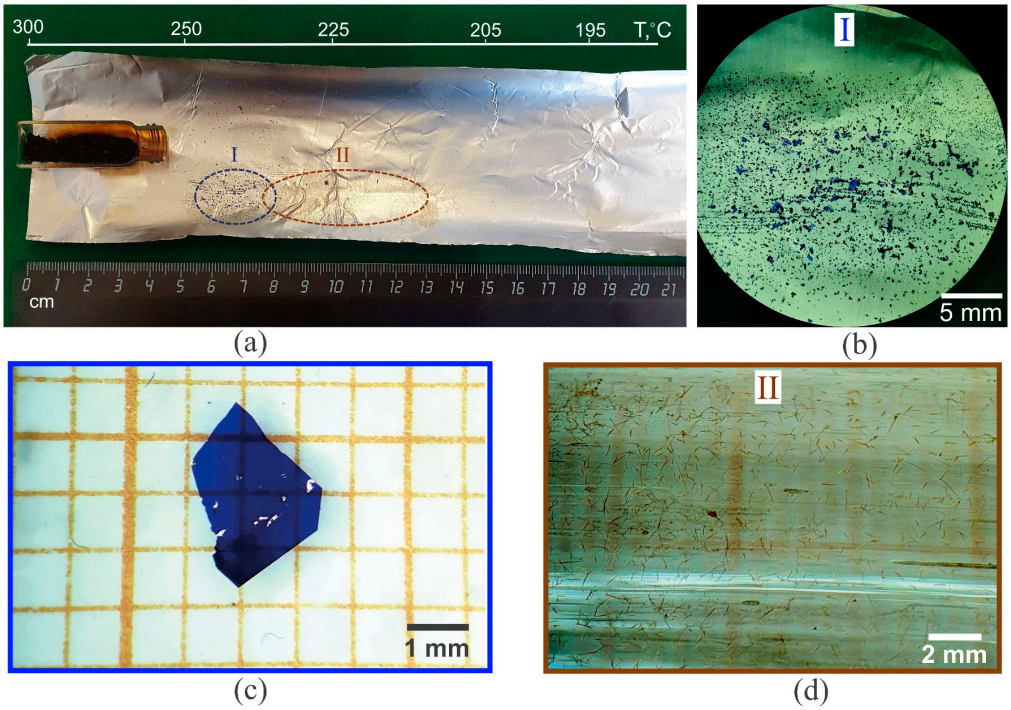


Figure 2. Crystals grown in a gradient temperature field: (**a**) the location of the source of the substance and areas of predominant precipitation of blue lamellar (I) and golden needle (II) crystals, indicating the temperature gradient in the growth experiment; (**b**) enlarged image of area I; (**c**) enlarged view of one of the larger pentacene crystals; (**d**) enlarged view of the area of deposition of golden needle crystals on the inner surface of the quartz growth tube.

In the second step, we investigated the crystallization of pentacene in a growth furnace with a two-zone thermal field. The temperature of the hot zone, T_1, was constant at 290 °C, and the temperature of the cold zone, T_2, was varied from 220 to 250 °C in increments of 10 degrees from experiment to experiment. The choice of the given temperature T_1 was due to the relatively high intensity of the sublimation processes of the substance, which made it possible to reduce the period of crystal growth from 10–14 days to 3 days. That is, this temperature was a compromise and slightly exceeded the threshold value determined by DSC (see Section 3.1). Under these conditions, there was a drastic change in the nature of deposition and crystal growth (Figure 3a). Intensive crystal growth occurred at the boundaries of thermal regime change. In the transition site between the hot and cold zones, the largest flat crystals of dark-blue color were formed (region I, Figures 3a and S3a–c). Crystal growth inside the cold zone (2) was not observed (Figure 3a).

With a change in the temperature of the cold zone, a change in the shape and thickness of the crystals was noted (Figure 3e). The largest flat dark-blue pentacene crystal, more than 1 cm wide and about 65 μm thick, was grown at a cold zone temperature T_2 = 220 °C (Figure 3e). With an increase in temperature T_2, on average, the length of the crystal decreased while the sides became more clearly faceted (Figure 3e, T_2 = 230 °C). At temperatures T_2 = 240–250 °C, an elongation of the shape of crystals and an increase in their thickness up to 250 μm were observed (Figure S3c). In general, with an increase in the temperature of the cold zone over the same period of growth, the average thickness of the largest crystal samples increased linearly (Figure S4).

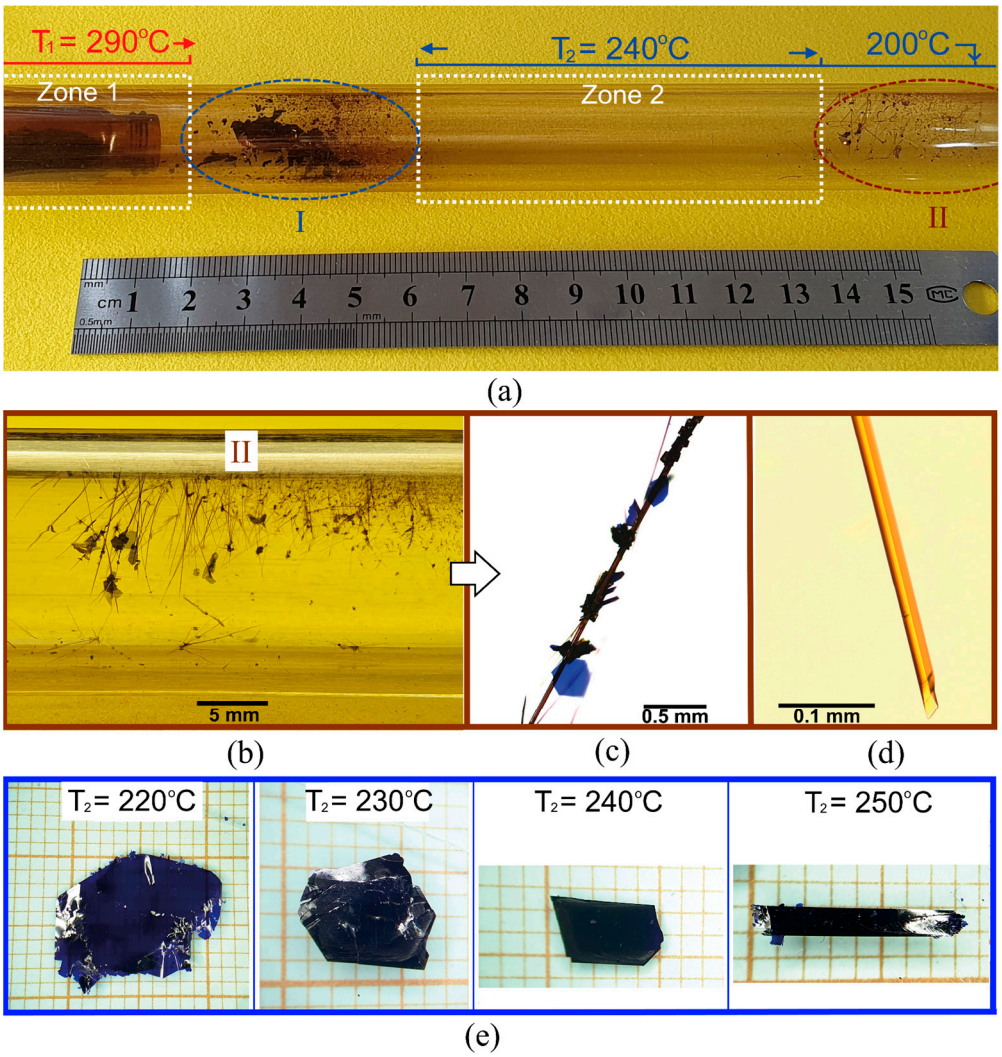


Figure 3. Crystals grown in a two-zone temperature field: (**a**) the location of the source of the substance and areas of predominant precipitation of dark-blue lamellar (I) and golden needle (II) crystals; (**b**) enlarged image of region II; (**c**,**d**) magnified images of a golden needle; (**e**) single crystals of pentacene on graph paper grown at different temperatures in the second (cold) zone.

To the right of the cold zone, a colony of golden needles was formed (region II, Figures 3a,b and S5). The lengths of the largest needles were up to 10 mm (Figure 3b). Outgrowths of dark-blue lamellar crystals were observed on some of them (Figures 3c and S5a). The lateral surface of the needle crystals was faceted (Figures 3d and S5b).

According to the elemental analysis, the oxygen content of the golden needle crystals was almost 10% higher than the background value (Figure S6). Thus, these crystals apparently consisted of oxidized pentacene molecules.

The developed faces of the flat and thin pentacene crystals often had smooth surfaces (Figures S2 and S3a). However, for large thick crystals, the developed face was rougher and characterized by the presence of many macro steps and inhomogeneities (Figure S3c,d). In some cases, regions with a smooth surface morphology were observed on the developed face of large Pc crystals. As an example, Figure 4a shows an AFM image of the surface of one of these crystals, on which elementary growth steps were observed corresponding with the thickness of the monolayer in an orientation parallel to the developed face of the crystal. The step height within the image region was ~1.5 ± 0.1 nm, which approximately corresponded with the thickness of a monolayer oriented parallel to the (0 0 1) plane [36,37].

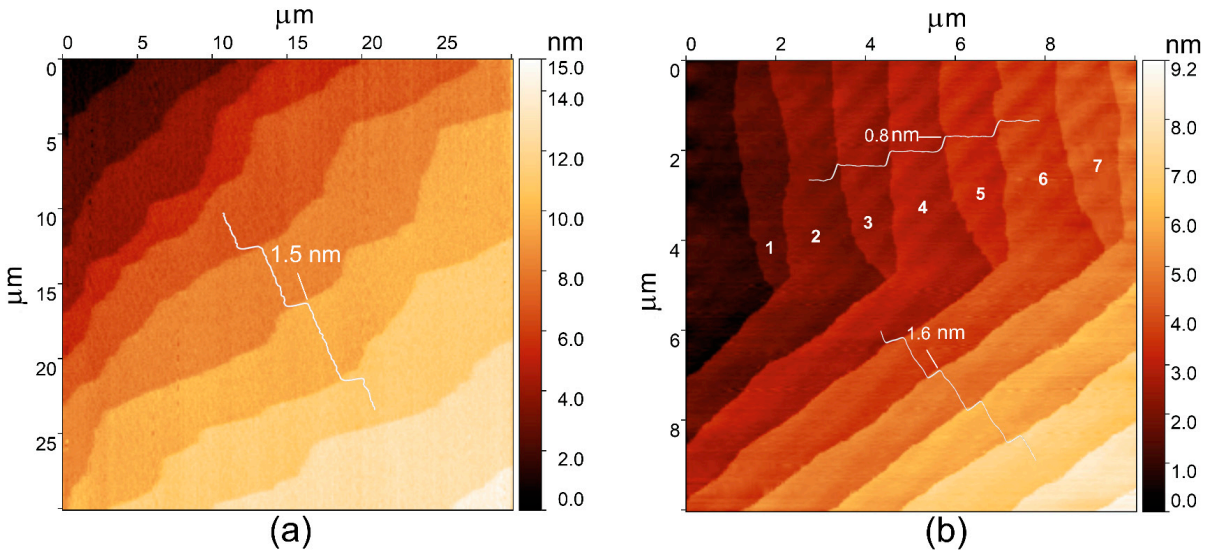


Figure 4. Topographic AFM images of surface areas of a dark-blue lamellar pentacene crystal (**a**) and a golden needle crystal (**b**).

A series of elementary growth steps was also observed on the developed smooth face of golden needle crystals (Figure 4b). A larger-scale AFM image of the surface with the scan area almost completely covering the width of the crystal is shown in Figure S5c (the area shown in Figure 4b is highlighted by a white dashed square). The needle crystal is oriented horizontally with respect to the image in Figure 4b. In the presented AFM topogram, in the lower part of the image, a parallel row of growth steps 1.6 ± 0.1 nm high with approximately the same terrace width ~1 μm can be observed. As one can see, the growth steps in the upper part of the image broke at an angle of 120–125 degrees and the widths of their terraces noticeably increased. In this case, a peculiarity was observed: a second intermediate row of steps appeared, the height of which was two times less. The front line of the conditionally even steps was close to a straight line, while the front line was rounded for the intermediate (odd) steps. Apparently, in this case, certain regularities of layer-by-layer growth were present, which determined the progression of either monolayers or bilayers of molecules at the crystallization front.

To explain the features of Pc crystallization in a two-zone thermal field, consider the schematic PT diagram shown in Figure 5, which depicts the regions of phase states near the crystal-vapor phase equilibrium line (blue line). Point 1 on the phase equilibrium line corresponds to the position of the source with the substance at temperature T_1 in the hot zone. Point 2 corresponds to the phase equilibrium point for a homogeneous temperature field inside the cold zone. The driving force of crystallization is the difference in chemical potentials, $\Delta\mu$, of the vapor (μ_v) and crystalline (μ_c) phases. On the phase equilibrium line, $\Delta\mu = 0$, and for a supersaturated vapor, the maximum value of $|\Delta\mu|$ determines the metastability boundary of vapor states (dashed red curve in Figure 5). The change in the value of $\Delta\mu$ with a change in pressure, P, and temperature, T, is determined by the following thermodynamic expression [38]:

$$\Delta\mu = \left(\frac{\partial\mu_v}{\partial P} - \frac{\partial\mu_c}{\partial P}\right)\Delta P + \left(\frac{\partial\mu_v}{\partial T} - \frac{\partial\mu_c}{\partial T}\right)\Delta T = (\Omega_v - \Omega_c)\Delta P + (S_v - S_c)\Delta T, \quad (1)$$

where Ω_v and Ω_c are the specific volumes per molecule for the vapor and crystal, respectively, and S_v and S_c are the entropies of the vapor and crystal phases, respectively.

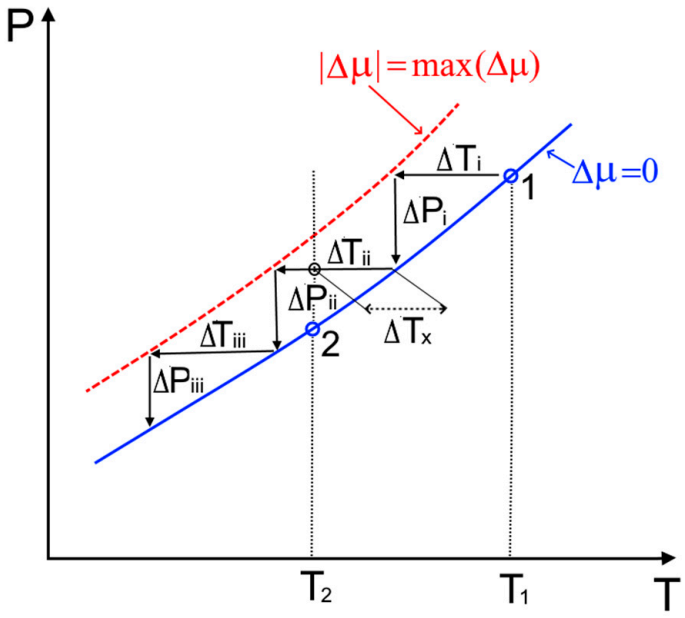


Figure 5. Schematic PT diagram explaining the features of crystallization of crystals via vapor in a two-zone growth setup. The blue curve is the line of crystal-vapor phase equilibrium, and the red dotted curve is the boundary of the metastability region of supersaturated vapor. Black arrows indicate the path of crystallization.

Consider the path of crystallization during evaporation and sublimation of a substance in a growth tube. The vapor phase, which is in equilibrium with the crystals at point 1, shifts to a colder region in the growth tube, gradually becoming supersaturated. In the phase diagram, the displacement of vapor towards lower temperatures occurs quasi-isobarically ($\Delta P \approx 0$), which corresponds to the horizontal section of the trajectory in Figure 5. At some supercooling ΔT_i, the vapor phase reaches the system metastability limit and the formation of crystals becomes inevitable. In this case, the magnitude of the driving force of crystallization can be determined as follows:

$$\Delta\mu \approx \Delta H_s \Delta T_i / T_1, \quad (2)$$

where $\Delta H_s = T_1(S_v - S_c)$ is the heat of sublimation at T_1. During mass crystallization, the pressure of supersaturated vapor decreases and approaches the equilibrium value isothermally (vertical section of the trajectory). Further, during isobaric cooling, the vapor phase is supercooled again, and the situation is repeated for lower values of pressure and temperature. Thus, in a simplified way, the path of crystallization of a substance on the phase diagram can be represented as a series of steps, each of which characterizes the formation and growth of crystals in a certain range of temperatures and pressures of supersaturated vapor.

Inside the cold zone, a homogeneous thermal field corresponds to the isotherm T_2 on the phase diagram. The vapor phase inside the cold zone is at a constant pressure, with a state of some constant supersaturation, ΔT_x, which can be characterized as conditionally stable or metastable ($\Delta\mu$ = const). This state can be exited by changing the parameters P and T. As a result, the formation and growth of crystals inside a homogeneous cold zone temperature field (which should ideally correspond to a point (2) in the phase diagram) are not observed. Therefore, the primary function of the cold quasi-isothermal zone in the growth tube is to establish the temperature gradient in the transition region for selecting optimal conditions for crystal growth.

3.3. Crystal Structure and Morphology

The main crystallographic parameters, experimental data, and the results of structure refinement of two single crystals (sample I—dark-blue lamellar crystal; sample II—golden needle crystal; Figure S6) at a temperature of 85 K are shown in Table 1. The search for unit cells in the two single crystals investigated resulted in the selection of a triclinic cell for sample I and a rhombic cell for sample II with the parameters given in Table 1, which allowed over 70% of the measured reflexes to be indexed. Information about the investigated structures was deposited in the Cambridge Structural Database (CCDC ## 2241890, 2270079).

Table 1. Crystallographic characteristics, experimental data, and refinement of crystal structures of pentacene (I) and its oxidized derivative (II).

Sample	I (Dark-Blue)	II (Golden)
Formula	$C_{22}H_{14}$	$C_{22}H_{12}O_2$
Temperature (K)	85	85
Space group	$P\bar{1}$	$P2_12_12_1$
Z	2	4
a (Å)	6.2818 (1)	3.88783 (4)
b (Å)	7.6478 (1)	12.4001 (0)
c (Å)	14.3514 (2)	28.9907 (8)
α (°)	76.958 (1)	90
β (°)	88.278 (1)	90
γ (°)	84.339 (1)	90
V (Å^3)	668.39 (2)	1397.62 (15)
Mr	278.4	308.3
D_X (g/cm^3)	1.383	1.465
μ (mm^{-1})	0.078	0.093
Radiation; λ (Å)	MoK_α; 0.71069	
Diffractometer	four-circle diffractometer XtaLAB Synergy R, DW system, HyPix-Arc 150 Hybrid Pixel Array Detector	
Scan type	ω	
Absorption correction; T_{min}/T_{max}	0.557/1.000	0.844/1.000
Θ_{max} (°)	48.67	48.78
No. of measured, independent, and observed [$I > 3\sigma(I)$] reflections	57,330, 6730, 5282	114,915, 2267, 1537
R_{int}	0.015	0.15
R/wR	0.024/0.031	0.055/0.052
S	1.83	2.15
$\Delta\rho_{min}/\Delta\rho_{max}$ (e·Å^{-3})	−0.19/0.25	−0.21/0.54

The refined parameters of the unit cell of the dark-blue lamellar crystals of pentacene (I) under our conditions corresponded well with the results of low-temperature research [39,40]. A view of the pentacene crystal's unit cell is shown in Figure 6a. According to the type of crystal structure, pentacene belongs to the group of linear conjugated molecules with a layered structure, in which the most densely packed layers of molecules oriented parallel to the (0 0 1) plane are superimposed on each other, resulting in a 2D anisotropic growth motif [41]. The thickness of the monolayer in the (0 0 1) plane orientation was h_{001} = 1.4 nm (Figure 6a), which corresponded with the height of the elementary growth step on the developed face of the Pc crystal determined by the AFM method (Figure 4a). The φ value of 125.6° was the herringbone angle of the stacked molecules inside the monolayers of (0 0 1). It was defined as the angle between the (5 12 15) and ($\bar{1}$0 24 15) planes (Figure 6b).

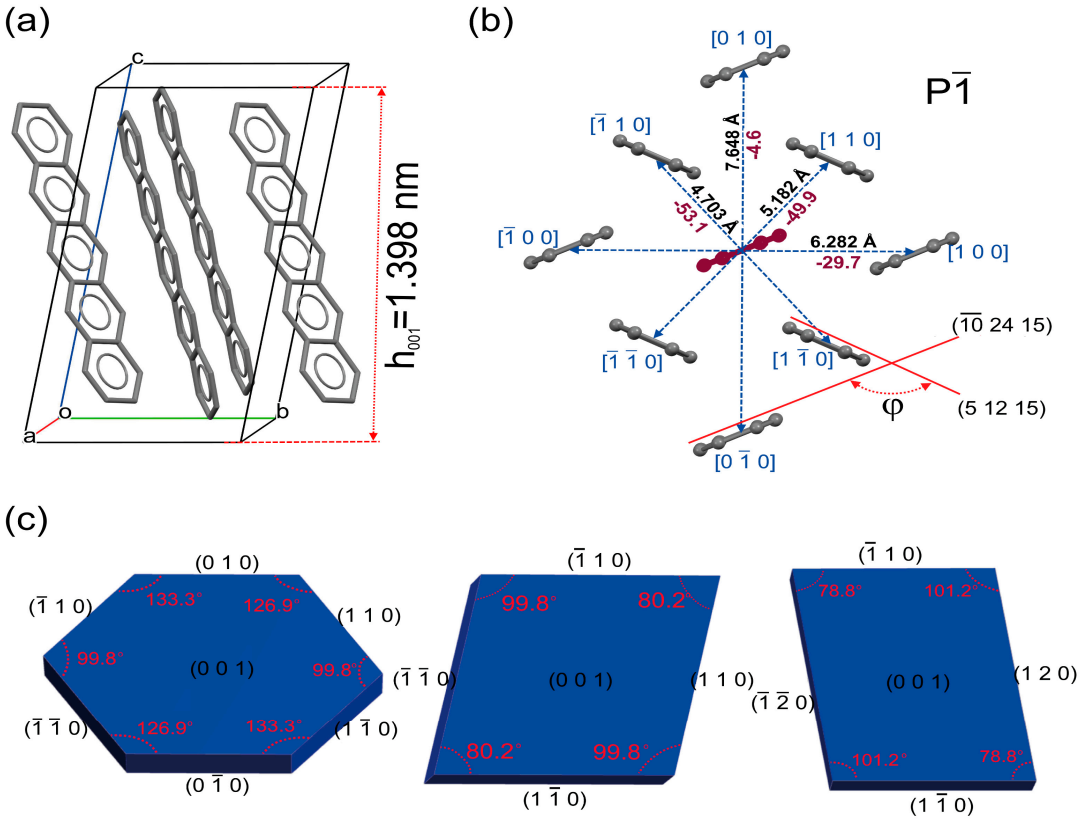


Figure 6. Crystal structure of pentacene at 85 K: (**a**) view of the unit cell; (**b**) scheme of molecules packing inside a monolayer in the (0 0 1) plane orientation, indicating the distances between the centers of molecules and the potentials of paired interactions in kJ/mol; (**c**) some simple shapes of flat crystals.

Figure 6b shows a fragment of a close-packed monolayer in the (0 0 1) plane orientation, consisting of a central molecule (highlighted in burgundy) and its nearest neighbors (first coordination). The presence of an inversion center indicated that the nature of the interaction between the central molecule and its nearest neighbors in the directions [1 0 0], [0 1 0], [1 1 0], and [1 $\bar{1}$ 0] was symmetrical for molecules located in opposite directions. In the diagram, the distances between the centers of molecules and the values of pair interaction potentials are indicated in the directions of bonds (highlighted in burgundy, kJ/mol). As can be seen, the strongest bond between molecules in the crystal occurred in the [1 $\bar{1}$ 0] direction, slightly weaker in the [1 1 0] direction, weaker in the [1 0 0] direction, and weakest in the [0 1 0] direction. Such anisotropy of the bonding of molecules in a close-packed monolayer during crystal growth apparently led to the formation of planar individuals elongated in the directions of the strongest bond ([1 $\bar{1}$ 0]) or adjacent to them ([1 $\bar{2}$ 0], [2 1 0]) (Figures 3e, S3 and S7a).

Some simple flat forms of pentacene crystals reconstructed with the WinXMorph software [42] are shown in Figure 6c. By comparing the angles between the lateral faces of ideal and real crystals, the crystallographic orientation of the faces of the latter could be established (Figure S3a,b).

The results of studying the golden needle crystals showed that they consists of molecules of 5,14-pentacenedione (PD). The calculated oxygen content in the compound $C_{22}H_{12}O_2$ was 10.38%, which agreed well with the elemental analysis data (Figure S6). The crystal was of rhombic syngony. A view of the unit cell of the crystal and the structural chemical formula of this compound are shown in Figure 7a,b, respectively. Thus, the golden needle crystals were a product of crystallization of impurities, the PD molecules, which crystallized predominantly in the colder region of the growth zone. The presence

of the PD impurity phase seemed to be associated with the oxidation of pentacene upon prolonged exposure to air. The synthesis of 5,14-pentacenedione was described in [43–45], but no information was found on the growth and crystal structure of this compound. In the crystal, the molecules of 5,14-pentacenedione, like the molecules of pentacene, had a flat conformational structure, but their density, D_X, was almost 6% higher (Table 1).

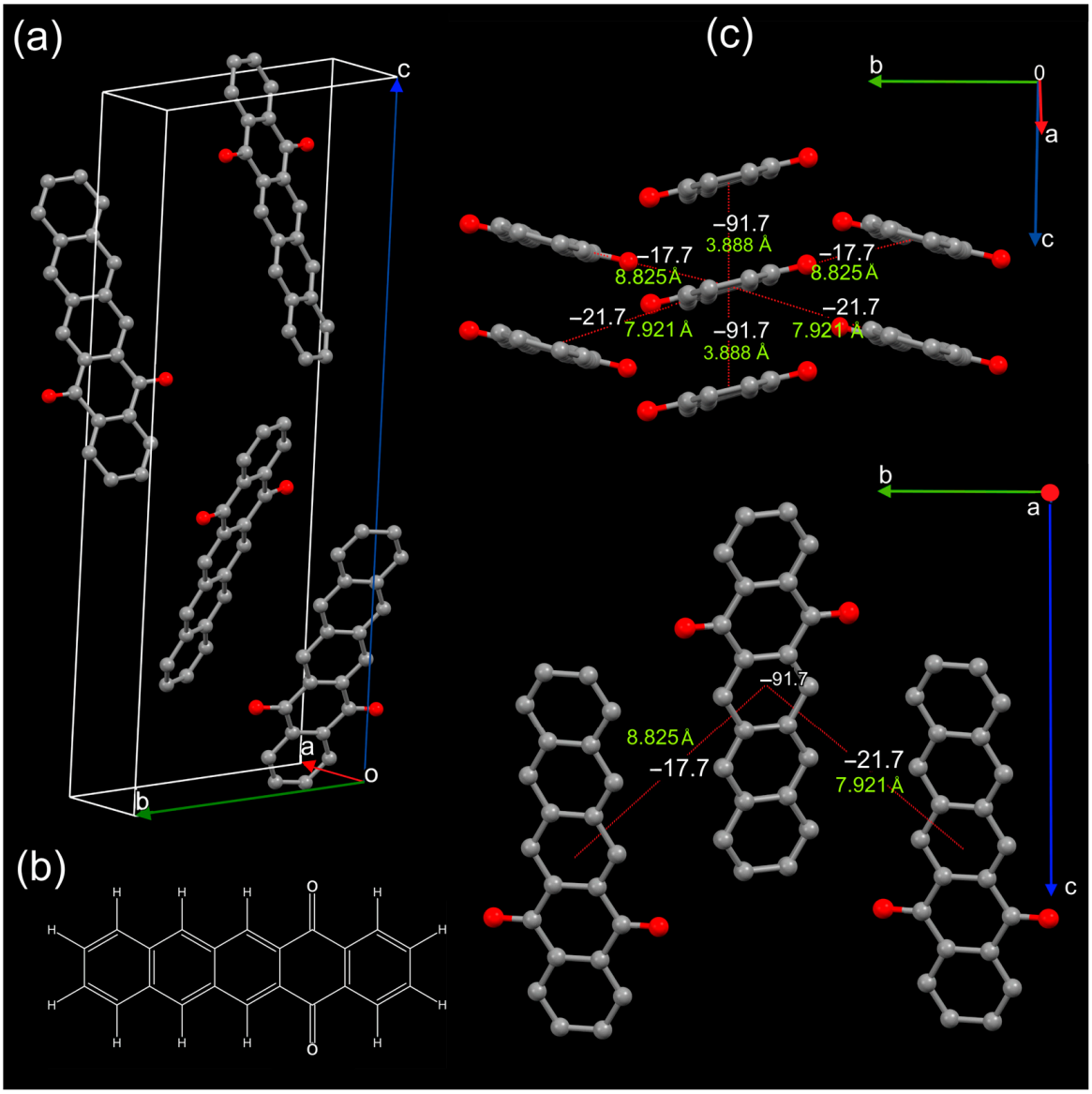


Figure 7. Crystal structure of 5,14-pentacenedione at 85 K: (**a**) view of the unit cell; (**b**) chemical structural formula of the compound; (**c**) diagram of the strongest interactions in the crystal between the nearest neighbors, with paired potentials (in kJ/mol) and distances between the centers of molecules indicated.

Figure 7c shows a diagram of the pair interaction potentials between the nearest neighbors in the crystal, calculated on the basis of the force field and the distances between their centers. The densest rows of molecules were oriented in the [1 0 0] direction and arranged in parallel stacks, resulting in strong intermolecular interactions between conjugated aromatic systems (3.888 Å, −91.7 kJ/mol). The anisotropic nature of the intermolecular interactions referred to the fact that they varied in strength depending on the direction of crystal growth. Specifically, the 1D anisotropy of PD crystal growth was determined by the neighboring densest rows of molecules being displaced from each other along the c-axis by approxi-

mately 0.4 molecular length, resulting in pair interactions between the nearest neighbors that were 4–5 times weaker in absolute value.

Calculations based on the force field of pairwise interaction potentials showed that the total energy of PD crystal packing was slightly higher in absolute value (186 kJ/mol) than in Pc crystals (170 kJ/mol).

In the unit cell, the molecular axis was parallel to either the (1 0 3) or ($\bar{1}$ 0 3) planes. The PD molecules formed a zigzag chain in the [0 0 1] direction when projected onto the (0 1 0) plane, with an angle of 136.2° between chain links defined as the angle between the (1 0 3) and ($\bar{1}$ 0 3) planes (Figure S8a). When projected onto the (1 0 0) plane, the densest molecular rows were stacked in a brickwork-type pattern (Figure 7b), which was typical for linear conjugated molecules that crystallize predominantly in the form of needles or rods [46,47].

Bilayer growth steps of about 1.6 nm in height (Figure 4b) detected on the developed lateral edge of the PD needle crystals seemed to characterize the surface micromorphology as high-index vicinal (Figure S7b), as the thicknesses of bilayers parallel to the low-index planes such as (0 1 0) and (0 1 2) (Figure S8b) did not satisfy the given value.

3.4. Optical Absorption and Luminescence Spectra

Figure 8 shows the normalized absorption and luminescence spectra of PD (curves 1a and 1b, respectively) and pentacene solutions (curves 2a and 2b, respectively). In the insert in Figure 8, the absorption spectra in the short-wavelength region are normalized to intense short-wavelength maxima.

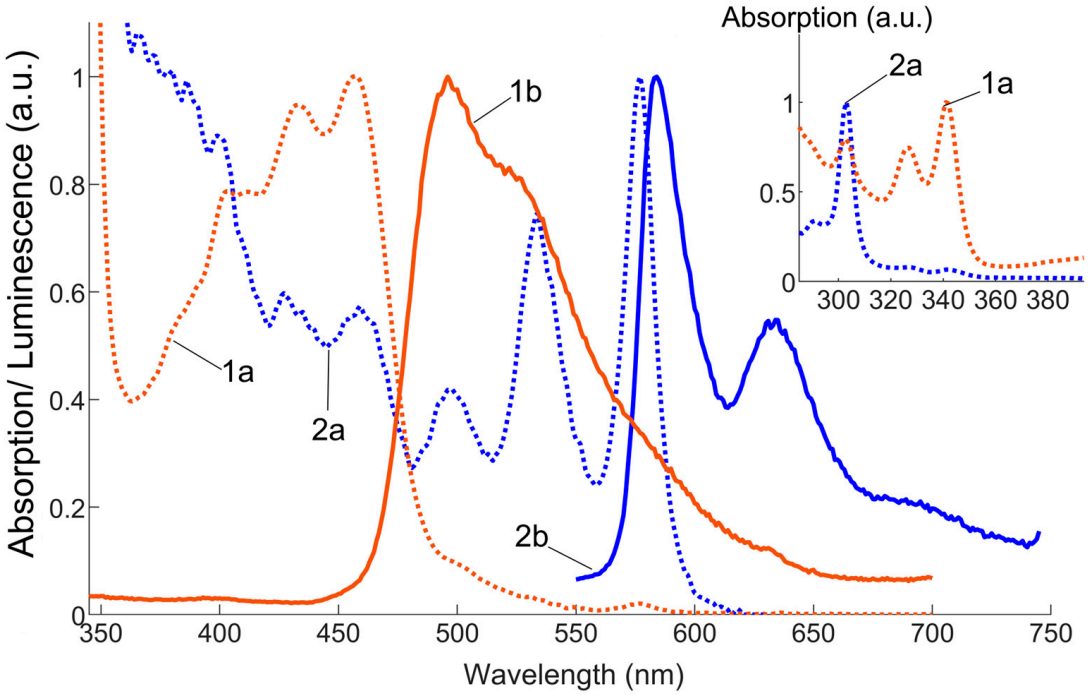


Figure 8. Maximum-normalized absorption spectra of solutions in toluene: curve 1a—PD (normalized to 1 at λ = 458 and 341 nm in the main plot and the insert, respectively); curve 2a—Pc (normalized to 1 at λ = 577 and 302 nm in the main plot and the insert, respectively). Luminescence spectra of solutions in toluene: curve 1b—PD; curve 2b—Pc (λ_{ex} = 302 and 533 nm, respectively).

The absorption spectrum of PD (curve 1a) showed a series of bands with maxima at 403, 432, and 456 nm. In the wavelength range up to 350 nm (curve 1a in the inset), a second series was observed with maxima at 303, 326, and 341 nm, the average optical density of which was 5–10 times higher than in the first series (λ > 350 nm). The luminescence spectrum of the PD solution (curve 1b) showed a band with a maximum at 496 nm and

a long-wavelength shoulder at 525 nm, which were symmetric with respect to the first series of absorption bands, and therefore corresponded to the S_0–S_1 transitions. The Stokes shift was at 1770 cm^{-1} and the 0-0 transition was at 476 nm. Fundamental changes in the shape of the luminescence spectrum upon excitation in the range from 303 to 456 nm were not observed.

The normalized at the maximum of 577 nm absorption spectrum of the pentacene solution is shown as curve 2a. The shape of the obtained spectrum matched well with the absorption spectrum of pentacene in benzene in terms of the positions of the maxima [48]. The luminescence spectrum of Pc solution obtained by excitation at λ_{ex} = 533 nm (curve 2b) had two characteristic bands at 583 and 634 nm, which is consistent with the data obtained in the THF [49].

3.5. Electrical Properties

Figure 9 shows the current–voltage characteristics of FETs fabricated using PVD-grown polycrystalline thin films of pentacene (Figures 9a,b and S8b) and PVT-grown 1.5 × 2.5 mm pentacene single crystals (Figures 9c,d and S8c). The electrical properties of FETs fabricated using pentacene crystals are shown in Table 2. For comparison, the parameters of FET devices taken from [2–4] are also given.

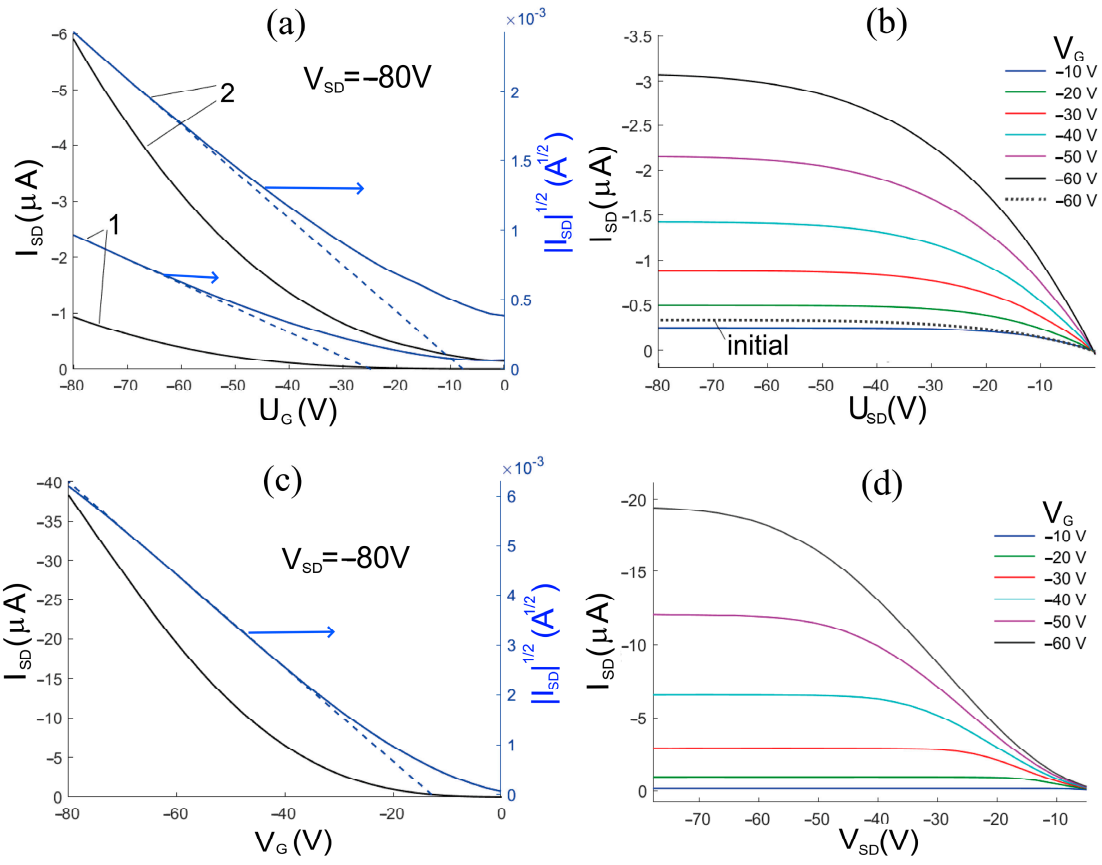


Figure 9. I–V characteristics of FET devices based on pentacene crystals: transfer (**a**) and output (**b**) curves for thermally deposited thin films based on the initial (1) and purified (2) substance; transfer (**c**) and output (**d**) curves for single crystals.

Table 2. Pentacene-based FET characteristics.

Active Layer	Ref.	Dielectric	Layer Thickness (nm)	$<d_{gr}>$ (nm)	W/L	μ_{sat} ($<\mu_{sat}>$) ($cm^2 \cdot V^{-1}s^{-1}$)	$<V_T>$ (V)
polycrystalline film (initial)	this work	SiO_2 (440 nm)	40 ± 10	130	10	0.01 (0.004 *)	−15 *
polycrystalline film (purified)	this work	SiO_2 (440 nm)	40 ± 10	180	5	0.07 (0.02 **)	−5 **
	[2]	PMMA/PVP (60 nm)	50	-	20	1.51	−20.1
		Si/SiO_2 (300 nm)/OTS	50	-	20	0.66	−12.3
Single crystal	this work	SiO_2 (440 nm) + PMMA (290 nm)	2300 ± 100	-	10	0.40 (0.10 ***)	−8 ***
	[3]	-	45	-	-	6.2 (5.5)	−37.5
	[4]	-	30–300	-	-	5.7 (2.0)	-

Note. $<d_{gr}>$ is average grain size; W and L are the length and width of the transistor channel, respectively; μ_{sat} and $<\mu_{sat}>$ are the maximum and average values of hole mobility in the saturation mode, respectively; $<V_T>$ is the average threshold voltage. * for 36 devices; ** for 106 devices; *** for 10 devices.

Curves 1 in Figure 9a characterize the properties of a polycrystalline Pc film based on the initial (unpurified) substance, while curves 2 are for purified pentacene. Since pentacene is practically insoluble and the impurities contained within it are more soluble, purification of the substance was carried out by preparing a suspension of the initial substance in toluene and keeping it in an ultrasonic bath at 50 °C for 0.5 h, followed by decantation after centrifugation (the procedure was performed 3 times). Due to active dissolution of the impurities, the decantate was colored orange-brown.

As can be seen from Figure 9a, the electrical characteristics significantly improved when using purified pentacene, which was also clearly visible in the FET output characteristics (Figure 9b and Figure S10). Thus, for polycrystalline layers with approximately the same thickness, the hole mobility increased by almost an order of magnitude and the threshold voltage decreased by a factor of three (Table 2).

A series of five FET devices based on needle-shaped PD single crystals was also produced (Figure S11a). For all samples, no transistor operation was observed due to the high resistivity of the crystals (Figure S11b). From this it can be concluded that in the PD molecular system the degree of delocalization of π-electrons was low for charge transfer between molecules in the crystal.

Figure 10 shows topographic AFM images of the surface of crystalline pentacene films in the FET channel. As can be seen, the crystalline film based on the initial (unpurified) pentacene (Figure 10a) had a finer grain structure than the film made from the purified substance (Figure 10b). For purified pentacene, the average grain size, $<d_{gr}>$, increased almost 1.4 times; correspondingly, the average grain density decreased by half (Table 2). Thus, the impurities present in commercial pentacene during vapor deposition on a substrate caused the formation of polycrystalline films with a finer-grained structure. Accordingly, in the FET channel in the direction of electric charge transfer between the source and the drain, the number of disordered inter-grain boundaries with high trap concentration was significantly higher, which caused serious degradation of the electrical performance of the thin pentacene films.

Due to the relatively large thickness of the pentacene single crystals (Table 2), the FET geometry used was not optimal to achieve the highest hole mobility; however, the μ_{sat} value in saturation mode was almost 6 times higher than that for the purified thin polycrystalline layers (Table 2). Thus, in terms of electrical properties, single crystals demonstrated the best performance.

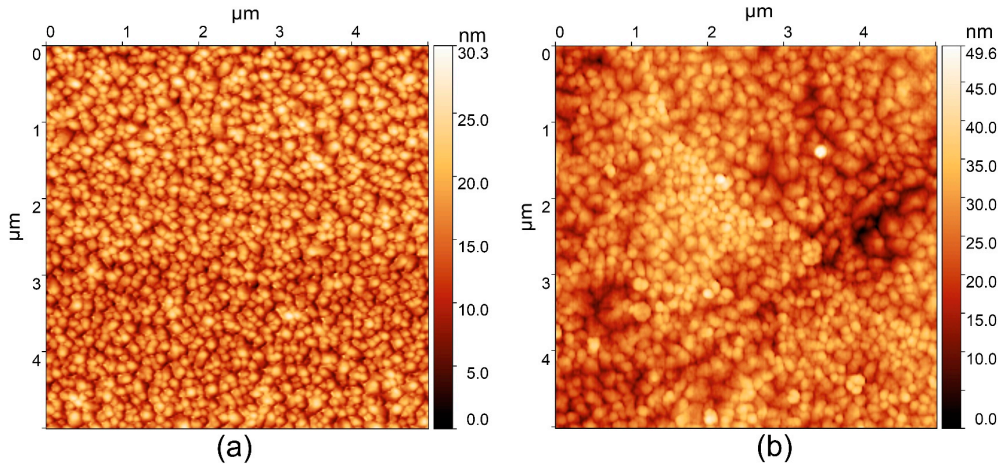


Figure 10. Topographic AFM surface images of pentacene crystalline films based on the initial (**a**) and purified (**b**) substance.

In this work, the goal was not to achieve high results for FETs based on pentacene single crystals, as was shown in [4] for example, but the presented examples demonstrated the advantages of organic semiconductor single crystals over polycrystalline thin films in charge transfer. In addition, the current–voltage characteristics shown in Figure 9a,b are a good illustration of the fact that PD impurities contained in the commercial pentacene material led to a decrease in the morphological quality of the polycrystalline thin films during PVD deposition (Figure 10) and in general significantly impaired the electrical properties of the crystals.

4. Conclusions

The use of a growth furnace with a two-zone thermal field showed high efficiency in producing centimeter-scale pentacene crystals and resulted in a clearer separation of the crystallization regions of pentacene from the impurity subsystem in comparison with the classical PVT method with a gradient thermal field. As it turned out, crystals were mainly deposited in areas with significant temperature gradients (between hot and cold zones and beyond their outer limits), and crystallization did not occur inside the cold zone, where the temperature field was quasi-uniform and the saturated vapor pressure remained practically unchanged. It was established that by changing the temperature of the cold zone, it was possible to influence the shape of flat pentacene crystals, obtaining individual crystals that were either uniformly wide and thin or elongated and thicker. Using this approach, it was possible to obtain pentacene semiconductor crystals of considerable size, which can serve as a platform for the development of optoelectronic devices with complex architectures. Using the method of single-crystal X-ray diffraction, the structure of flat dark-blue pentacene crystals in a triclinic system with sp.gr. $P\bar{1}$ was refined. Crystals of 5,14-pentacenedione deposited in the colder region of the growth furnace as golden needles with lengths up to 10 mm and thicknesses up to 50 microns were obtained, and their crystal structure was established as a rhombic system with sp.gr. $P2_12_12_1$. The presence of this compound as an impurity is most likely associated with the degradation of pentacene in air during storage. The absorption and luminescence spectra of 5,14-pentacenedione in toluene solution compared to those of pentacene were significantly shifted to the short-wavelength region. The 5,14-pentacenedione absorption band had a strong vibrational structure with maxima at 403, 432, and 456 nm, and the luminescence spectrum was mirrored and symmetric in shape with a maximum at 496 nm and a long-wavelength shoulder at 525 nm. The field-effect transistor study of the electrical properties of thin polycrystalline pentacene films showed that the presence of the 5,14-pentacenedione impurity phase in the composition of commercial high-purity material negatively affected the electrical transport characteristics. Purification of pentacene by

separating the insoluble precipitate upon treatment with toluene significantly improved the electrical properties of thin polycrystalline films in the structure of FET devices: the hole mobility in the saturation mode, μ_{sat}, increased by almost an order of magnitude and the threshold voltage, V_T, decreased by several times. Compared to thin polycrystalline layers, pentacene single crystals exhibited significantly higher hole mobility in FET devices.

Supplementary Materials: The following supporting information can be downloaded at: https://www.mdpi.com/article/10.3390/cryst13070999/s1, Figure S1: DSC curve of pentacene sample in sealed crucible; Figure S2: Pentacene crystals grown in a gradient thermal field; Figure S3: Crystals grown in a two-zone thermal field: (a), (b) flat Pc crystals with angles between faces and indexes of faces indicated; (c) elongated lamellar Pc crystals; (d) enlarged confocal image of surface of thick Pc crystal; Figure S4: The dependence of the average thickness of the largest pentacene crystals in the growth zone on the temperature of the cold zone; Figure S5: Images of golden needle crystals: (a) collection of needle-shaped crystals with dark-blue lamellar crystals on some of them; (b) enlarged optical image of crystal tip; Figure S6: Elemental analysis of a golden needle crystal: (a) SEM image of crystal; (b) EDS elemental spectroscopy at the position shown in (a); (c) distribution of carbon and oxygen atoms inside (2) and outside the crystal (1,3); Figure S7: Images of a single crystals of pentacene (a) and PD (b) with face indices determined in the X-ray diffraction experiment; Figure S8: PD crystal structure model at 85 K: projections of the structure on the planes (010) (a) and (100) (b); Figure S9: Diagram of the field-effect transistor device (a); photo-images of pentacene-based field-effect transistors based on thermally deposited polycrystalline layer (b) and single crystal (c); Figure S10: Output I–V characteristics for a thin polycrystalline layer based on the initial (unpurified) pentacene; Figure S11: Photo-image of a field-effect transistor based on a PD single crystal (a) and its I–V transfer characteristic ($V_{SD} = -80$ V); CIF S1: Crystal structure of Pc at 85 K; CIF S2: Crystal structure of PD at 85 K.

Author Contributions: Conceptualization and writing—original draft preparation, V.A.P.; methodology, A.A.K., G.A.Y., N.I.S., T.A.S., V.V.G. and V.A.P.; DSC/TG, V.V.G.; crystal growth and optical microscopy, A.A.K.; SCXRD, T.A.S. and N.I.S.; optical spectroscopy, G.A.Y.; FET fabrication and electro-physical measurements, G.A.Y.; AFM, G.A.Y.; writing—review and editing, V.A.P., G.A.Y., V.V.G. and N.I.S. All authors have read and agreed to the published version of the manuscript.

Funding: This work is supported by the Ministry of Science and Higher Education within a state assignment for the Federal Scientific Research Centre "Crystallography and Photonics" of the Russian Academy of Sciences.

Data Availability Statement: Not applicable.

Acknowledgments: The research was carried out using equipment of the Shared Research Center "Structural Diagnostics of Materials" of the FSRC "Crystallography and Photonics" RAS. The authors are grateful to Alexey Voloshin for discussion of the work and useful comments and to Yuriy Grigoriev and Ivan Volchkov for conducting the elemental analysis.

Conflicts of Interest: The authors declare no conflict of interest.

Appendix A

The mobility of the charge carrier, μ_{sat}, in the saturation mode was determined on the basis of the current value between the source and drain, I_{SD}, obtained by measuring the voltage at the gate, $V_{G,}$ using the expression:

$$I_{SD} = \frac{W}{2L}\mu C(V_G - V_T)^2, \quad \text{(A1)}$$

where W and L are the width and length of the transistor channel, respectively; and C = 7.3 nF/cm^2 is the specific surface electrical capacity of the gate dielectric (to estimate the value of C, permittivity values $\varepsilon_{SiO2} = 3.9$ and $\varepsilon_{PMMA} = 3.6$ were used).

References

1. Zhang, X.H.; Domercq, B.; Wang, X.; Yoo, S.; Kondo, T.; Wang, Z.L.; Kippelen, B. High-Performance Pentacene Field-Effect Transistors Using Al_2O_3 Gate Dielectrics Prepared by Atomic Layer Deposition (ALD). *Org. Electron.* **2007**, *8*, 718–726. [CrossRef]
2. Yi, M.; Guo, J.; Li, W.; Xie, L.; Fan, Q.; Huang, W. High-Mobility Flexible Pentacene-Based Organic Field-Effect Transistors with PMMA/PVP Double Gate Insulator Layers and the Investigation on Their Mechanical Flexibility and Thermal Stability. *RSC Adv.* **2015**, *5*, 95273–95279. [CrossRef]
3. Kang, B.; Jang, M.; Chung, Y.; Kim, H.; Kwak, S.K.; Oh, J.H.; Cho, K. Enhancing 2D Growth of Organic Semiconductor Thin Films with Macroporous Structures via a Small-Molecule Heterointerface. *Nat. Commun.* **2014**, *5*, 4752. [CrossRef] [PubMed]
4. Dong, J.; Yu, P.; Arabi, S.A.; Wang, J.; He, J.; Jiang, C. Enhanced Mobility in Organic Field-Effect Transistors Due to Semiconductor/Dielectric IInterface Control and Very Thin Single Crystal. *Nanotechnology* **2016**, *27*, 275202. [CrossRef] [PubMed]
5. Kim, H.S.; Kim, S.; Koo, J.Y.; Choi, H.C. Highly Pure Pentacene Crystals Grown by Physical Vapor Transport: The Critical Role of the Carrier Gas. *J. Mater. Chem. C* **2021**, *9*, 1911–1917. [CrossRef]
6. Ruiz, R.; Choudhary, D.; Nickel, B.; Toccoli, T.; Chang, K.C.; Mayer, A.C.; Clancy, P.; Blakely, J.M.; Headrick, R.L.; Iannotta, S.; et al. Pentacene Thin Film Growth. *Chem. Mater.* **2004**, *16*, 4497–4508. [CrossRef]
7. Wang, H.; Li, F.; Gao, B.; Xie, Z.; Liu, S.; Wang, C.; Hu, D.; Shen, F.; Xu, Y.; Shang, H.; et al. Doped Organic Crystals with High Efficiency, Color-Tunable Emission toward Laser Application. *Cryst. Growth Des.* **2009**, *9*, 4945–4950. [CrossRef]
8. Fan, C.L.; Lin, W.C.; Chang, H.S.; Lin, Y.Z.; Huang, B.R. Effects of the F4TCNQ-Doped Pentacene Interlayers on Performance Improvement of Top-Contact Pentacene-Based Organic Thin-Film Transistors. *Materials* **2016**, *9*, 46. [CrossRef]
9. Kabakchiev, A.; Kuhnke, K.; Lutz, T.; Kern, K. Electroluminescence from Individual Pentacene Nanocrystals. *ChemPhysChem* **2010**, *11*, 3412–3416. [CrossRef]
10. Zhao, Y.; Wang, L.; Chen, X.; Zhang, B.; Shen, F.; Song, H.; Wang, H. A High-Mobility, High-Luminescence and Low-Threshold Pentacene-Doped Cyano-Substituted Distyrylbenzene Crystal. *J. Mater. Chem. C* **2019**, *7*, 13447–13453. [CrossRef]
11. Takeyama, Y.; Maruyama, S.; Matsumoto, Y. Growth of Single-Crystal Phase Pentacene in Ionic Liquids by Vacuum Deposition. *Cryst. Growth Des.* **2011**, *11*, 2273–2278. [CrossRef]
12. Kulishov, A.A.; Yurasik, G.A.; Grebenev, V.V.; Postnikov, V.A. Tetracene Crystals: Growth from Solutions, Solubility, and Thermal Properties. *Crystallogr. Rep.* **2022**, *67*, 1001–1012. [CrossRef]
13. Mattheus, C.C.; Dros, A.B.; Baas, J.; Meetsma, A.; De Boer, J.L.; Palstra, T.T.M. Polymorphism in Pentacene. *Acta Cryst. C* **2001**, *57*, 939–941. [CrossRef] [PubMed]
14. Kim, S.H.; Jang, M.; Yang, H.; Park, C.E. Effect of Pentacene-Dielectric Affinity on Pentacene Thin Film Growth Morphology in Organic Field-Effect Transistors. *J. Mater. Chem.* **2010**, *20*, 5612–5620. [CrossRef]
15. Yang, X.; Li, M.; Maeno, A.; Yanase, T.; Yokokura, S.; Nagahama, T. Growth of Pentacene Crystals by Naphthalene Flux Method. *ACS Omega* **2022**, *7*, 28618–28623. [CrossRef] [PubMed]
16. Lee, J.Y.; Roth, S.; Park, Y.W. Anisotropic Field Effect Mobility in Single Crystal Pentacene. *Appl. Phys. Lett.* **2006**, *88*, 252106. [CrossRef]
17. Laudise, R.; Kloc, C.; Simpkins, P.G.; Siegrist, T. Physical Vapor Growth of Organic Semiconductors. *J. Cryst. Growth* **1998**, *187*, 449–454. [CrossRef]
18. Roberson, L.B.; Kowalik, J.; Tolbert, L.M.; Kloc, C.; Zeis, R.; Chi, X.; Fleming, R.; Wilkins, C. Pentacene Disproportionation during Sublimation for Field-Effect Transistors. *J. Am. Chem. Soc.* **2005**, *127*, 3069–3075. [CrossRef]
19. Jo, S.; Takenaga, M. Morphologies of Pentacene Crystals Obtained by Physical Vapor Growth Technique. *Jpn. J. Appl. Phys.* **2010**, *49*, 078002. [CrossRef]
20. Jo, S.; Kajiwara, K.; Takenaga, M. Growth Process of Pentacene Crystals Obtained by Physical Vapor Transport Technique. *Jpn. J. Appl. Phys.* **2014**, *53*, 115506. [CrossRef]
21. Park, J.E.; Son, M.; Hong, M.; Lee, G.; Choi, H.C. Crystal-Plane-Dependent Photoluminescence of Pentacene 1da Wire and 2da Disk Crystals. *Angew. Chemie* **2012**, *124*, 6489–6494. [CrossRef]
22. Chen, K.Y.; Hsieh, H.H.; Wu, C.C.; Hwang, J.J.; Chow, T.J. A New Type of Soluble Pentacene Precursor for Organic Thin-Film Transistors. *Chem. Com.* **2007**, *10*, 1065–1067. [CrossRef]
23. Fulem, M.; Laštovka, V.; Straka, M.; Růžička, K.; Shaw, J.M. Heat Capacities of Tetracene and Pentacene. *J. Chem. Eng. Data* **2008**, *53*, 2175–2181. [CrossRef]
24. Postnikov, V.A.; Sorokina, N.I.; Lyasnikova, M.S.; Kulishov, A.A.; Voloshin, A.E.; Borshchev, O.V.; Surin, N.M.; Svidchenko, E.A.; Ponomarenko, S.A. Large Area Free-Standing Single Crystalline Films of p-Quinquephenyl: Growth, Structure and Photoluminescence Properties. *Crystals* **2020**, *10*, 363. [CrossRef]
25. Okada, Y.; Uno, M.; Nakazawa, Y.; Sasai, K.; Matsukawa, K.; Yoshimura, M.; Kitaoka, Y.; Mori, Y.; Takeya, J. Low-Temperature Thermal Conductivity of Bulk and Film-like Rubrene Single Crystals. *Phys. Rev. B Condens. Matter Mater. Phys.* **2011**, *83*, 113305. [CrossRef]
26. Ma, L.; Zhang, K.; Kloc, C.; Sun, H.; Michel-Beyerle, M.E.; Gurzadyan, G.G. Singlet Fission in Rubrene Single Crystal: Direct Observation by Femtosecond Pump-Probe Spectroscopy. *Phys. Chem. Chem. Phys.* **2012**, *14*, 8307–8312. [CrossRef]
27. Park, C.; Park, J.E.; Choi, H.C. Crystallization-Induced Properties from Morphology-Controlled Organic Crystals. *Acc. Chem. Res.* **2014**, *47*, 2353–2364. [CrossRef]

28. Courté, M.; Ye, J.; Jiang, H.; Ganguly, R.; Tang, S.; Kloc, C.; Fichou, D. Tuning the π-π Overlap and Charge Transport in Single Crystals of an Organic Semiconductor: Via Solvation and Polymorphism. *Phys. Chem. Chem. Phys.* **2020**, *22*, 19855–19863. [CrossRef] [PubMed]
29. *Gwiddion*, version 2.59; Software for scanning probe microscopy data visualization and analysis; Czech Metrology Institute: Jihlava, Czech, 2020.
30. *CrysAlisPro*, version 171.41_64.88a; Software for single crystal X-ray diffraction; Rigaku Corporation: Tokyo, Japan, 2018.
31. Petrícek, V.; Dušek, M.; Palatinus, L. Crystallographic Computing System JANA2006: General Features. *Zeitschrift Krist.* **2014**, *229*, 342–345.
32. Palatinus, L. Ab Initio Determination of Incommensurately Modulated Structures by Charge Flipping in Superspace. *Acta Cryst. A* **2004**, *60*, 604–610. [CrossRef]
33. *Mercury*, version 2022.2.0; Software for Crystal Structure Visualization, Exploration and Analysis; The Cambridge Crystallographic Data Centre: Cambridge, UK, 2022.
34. Gavezzotti, A. Are Crystal Structures Predictable? *Acc. Chem. Res.* **1994**, *27*, 309–314. [CrossRef]
35. Tsumura, A.; Koezuka, H.; Ando, T. Macromolecular Electronic Device: Field-Effect Transistor with a Polythiophene Thin Film. *Appl. Phys. Lett.* **1986**, *49*, 1210–1212. [CrossRef]
36. Campbell, R.B.; Robertson, J.M.; Trotter, J. The Crystal Structure of Hexacene, and a Revision of the Crystallographic Data for Tetracene. *Acta Cryst.* **1962**, *15*, 289. [CrossRef]
37. Schiefer, S.; Huth, M.; Dobrinevski, A.; Nickel, B. Determination of the Crystal Structure of Substrate-Induced Pentacene Polymorphs in Fiber Structured Thin Films. *J. Am. Chem. Soc.* **2007**, *129*, 10316–10317. [CrossRef]
38. Chernov, A.A. *Madern Crystallography III: Crystal Growth*; Springer: Berlin/Heidelberg, Germany, 1984; ISBN 978-3-642-81837-0.
39. Haas, S.; Batlogg, B.; Besnard, C.; Schiltz, M.; Kloc, C.; Siegrist, T. Large Uniaxial Negative Thermal Expansion in Pentacene Due to Steric Hindrance. *Phys. Rev. B Condens. Matter Mater. Phys.* **2007**, *76*, 205203. [CrossRef]
40. Yanase, T.; Tanoguchi, H.; Sakai, N.; Jin, M.; Yamane, I.; Kato, M.; Ito, H.; Nagahama, T.; Shimada, T. Single Crystal Growth of π-Conjugated Large Molecules without Solubilizing Alkyl Chains via the Naphthalene Flux Method. *Cryst. Growth Des.* **2021**, *21*, 4683–4689. [CrossRef]
41. Postnikov, V.A.; Lyasnikova, M.S.; Kulishov, A.A.; Sorokina, N.I.; Voloshin, A.E.; Skorotetcky, M.S.; Borshchev, O.V.; Ponomarenko, S.A. Growth Anisotropy and Crystal Structure of Linear Conjugated Oligomers. *Phys. Solid State* **2019**, *61*, 2322–2325. [CrossRef]
42. Kaminsky, W. From CIF to Virtual Morphology Using the WinXMorph Program. *J. Appl. Cryst.* **2007**, *40*, 382–385. [CrossRef]
43. Laduranty, J.; Lepage, L.; Lepage, Y. Capture Du Paradiméthoxyorthoquinodiméthane: Synthèses de Quinones et d'un Intermédiaire de La Daunomycinone. *Can. J. Chem.* **1980**, *58*, 1161–1167. [CrossRef]
44. Smith, J.G.; Dibble, P.W.; Sandborn, R.E. The Preparation and Reactions of Naphtho[l,2-c]Furan and Naphtho[2,3-c]Furan. *J. Org. Chem.* **1986**, *51*, 3762–3768. [CrossRef]
45. Nishina, Y.; Kida, T.; Ureshino, T. Facile Sc(OTf)3-Catalyzed Generation and Successive Aromatization of Isobenzofuran from o -Dicarbonylbenzenes. *Org. Lett.* **2011**, *13*, 3960–3963. [CrossRef] [PubMed]
46. Postnikov, V.A.; Sorokina, N.I.; Kulishov, A.A.; Lyasnikova, M.S.; Grebenev, V.V.; Voloshin, A.E.; Borshchev, O.V.; Skorotetcky, M.S.; Surin, N.M.; Svidchenko, E.A.; et al. Highly Luminescent Crystals of a Novel Linear π-Conjugated Thiophene-Phenylene Co-Oligomer with a Benzothiadiazole Fragment. *Acta Cryst. B* **2019**, *75*, 1076–1085. [CrossRef] [PubMed]
47. Postnikov, V.A.; Sorokina, N.I.; Kulishov, A.A.; Lyasnikova, M.S.; Sorokin, T.A.; Freidzon, A.Y.; Stepko, A.S.; Borshchev, O.V.; Skorotetsky, M.S.; Surin, N.M.; et al. A New Linear Phenyloxazole–Benzothiadiazole Luminophore: Crystal Growth, Structure and Fluorescence Properties. *Acta Cryst. B* **2022**, *78*, 261–269. [CrossRef]
48. Hellner, C.; Lindqvist, L.; Roberge, P.C. Absorption Spectrum and Decay Kinetics of Triplet Pentacene in Solution, Studied by Flash Photolysis. *J. Chem. Soc., Faraday Trans. 2* **1972**, *68*, 1928–1937. [CrossRef]
49. Shimizu, A.; Ito, A.; Teki, Y. Photostability Enhancement of the Pentacene Derivative Having Two Nitronyl Nitroxide Radical Substituents. *Chem. Com.* **2016**, *52*, 2889–2892. [CrossRef]

Disclaimer/Publisher's Note: The statements, opinions and data contained in all publications are solely those of the individual author(s) and contributor(s) and not of MDPI and/or the editor(s). MDPI and/or the editor(s) disclaim responsibility for any injury to people or property resulting from any ideas, methods, instructions or products referred to in the content.